Formation pathways of Precambrian sedimentary pyrite: Insights from in situ Fe isotopes

Juliette Dupeyron, Marie-Noëlle Decraene, Johanna Marin-Carbonne, Vincent Busigny

▶ **To cite this version:**

Juliette Dupeyron, Marie-Noëlle Decraene, Johanna Marin-Carbonne, Vincent Busigny. Formation pathways of Precambrian sedimentary pyrite: Insights from in situ Fe isotopes. Earth and Planetary Science Letters, 2023, 609, pp.118070. 10.1016/j.epsl.2023.118070 . hal-04102180

HAL Id: hal-04102180

https://u-paris.hal.science/hal-04102180

Submitted on 22 May 2023

HAL is a multi-disciplinary open access archive for the deposit and dissemination of scientific research documents, whether they are published or not. The documents may come from teaching and research institutions in France or abroad, or from public or private research centers.

L'archive ouverte pluridisciplinaire **HAL**, est destinée au dépôt et à la diffusion de documents scientifiques de niveau recherche, publiés ou non, émanant des établissements d'enseignement et de recherche français ou étrangers, des laboratoires publics ou privés.

Earth and Planetary Science Letters 609 (2023) 118070

Contents lists available at ScienceDirect

Earth and Planetary Science Letters

journal homepage: www.elsevier.com/locate/epsl

Frontiers paper

Formation pathways of Precambrian sedimentary pyrite: Insights from *in situ* Fe isotopes

Juliette Dupeyron [a,b,*], Marie-Noëlle Decraene [a], Johanna Marin-Carbonne [a], Vincent Busigny [b,c]

[a] Institut des Sciences de la Terre, Universite de Lausanne, Lausanne, 1015, Switzerland
[b] Universite Paris Cite, Institut de Physique du Globe, CNRS, Paris, F-75005, France
[c] Institut Universitaire de France, Paris, 75005, France

ARTICLE INFO

Article history:
Received 11 July 2022
Received in revised form 9 January 2023
Accepted 15 February 2023
Available online xxxx
Editor: B. Wing

Keywords:
pyrite
Archean
Fe isotope composition
SIMS

ABSTRACT

Iron isotope compositions (expressed as δ^{56}Fe) in sedimentary pyrite have been widely used as tracers of redox and chemical evolution of the ocean through geological time. Previous studies mostly built on the mechanical extraction of sulfides from bulk rock samples, and focused on visible macroscopic pyrites, which may introduce a sampling bias. *In situ* analyses of micropyrite grains can provide new insights into the processes of pyrite formation and their time evolution. Here, we compile *ca.* 2000 *in situ* iron isotope compositions of Archean to Paleoproterozoic sedimentary pyrite, from previous literature as well as new data. Contrasting with bulk analyses, micropyrite displays a large and constant range of δ^{56}Fe values, from -4 to +4‰, through time. Micropyrite δ^{56}Fe values are not significantly influenced by metamorphic grade. A bimodal distribution of positive *versus* negative δ^{56}Fe values can be attributed to two different processes of pyrite formation, Fe (oxyhydr)oxide sulfidation, *versus* kinetic and possibly microbially mediated pyrite precipitation. These processes are tightly related to rock lithology and thus to sedimentary conditions, and have existed since 3.8 Ga.

© 2023 The Author(s). Published by Elsevier B.V. This is an open access article under the CC BY license (http://creativecommons.org/licenses/by/4.0/).

1. Introduction

Iron (Fe) was a dominant chemical element of the early ocean, as illustrated by the deposition of abundant Fe-rich sedimentary rocks such as banded iron formations (BIFs) through the Archean (Klein, 2005; Bekker et al., 2010; Konhauser et al., 2017). Fe played a key role in the development of early life (Lyons et al., 2015), and likely supported microbial activity, in particular anoxygenic photosynthesis and dissimilatory iron reduction (DIR). Some microorganisms can use Fe(II) as an electron donor for anoxygenic photosynthetic carbon fixation, others use Fe(III) as an electron acceptor in anaerobic respiration (Johnson and Beard, 2006). Phylogenetic studies highlight the great degree of conservation of genes responsible for most metabolic reactions involving Fe, suggesting that they evolved close to the root in the tree of life (Lonergan et al., 1996). Moreover, iron metabolic activities can induce Fe isotope fractionation, which can be recorded in Fe mineral phases through the geological record (Johnson et al., 2008). DIR signatures were evidenced in sedimentary sulfides as old as 3.28 Ga (Marin-Carbonne et al., 2020) and more broadly at 2.7 Ga (Archer and Vance, 2006; Craddock and Dauphas, 2011), while fingerprints of anoxygenic photosynthesis have also been reported in the Archean sedimentary record (Czaja et al., 2013; Rego et al., 2021). Significant Fe isotope fractionations occur during oxidation of Fe(II) to Fe(III) (Welch et al., 2003; Balci et al., 2006) and reduction of iron (oxyhydr)oxides (Crosby et al., 2005, 2007; Wiederhold et al., 2006; Frierdich et al., 2019). Therefore, Fe isotope composition has been extensively used as a proxy for reconstructing redox and chemical evolution of the ocean, together with co-evolution of early living organisms (see review in Anbar and Rouxel, 2007; Johnson et al., 2008; Dauphas et al., 2017).

In a pioneer work, Rouxel et al. (2005) measured bulk Fe isotope composition of pyrite grains in black shales, from late Archean to Paleoproterozoic, and discovered a negative isotope excursion (*i.e.*, enrichment in light Fe isotopes) just before the Great Oxygenation Event (GOE, 2.4 Ga; Bekker et al., 2004). The negative δ^{56}Fe values recorded in Neoarchean pyrite were interpreted as inherited from extensive seawater Fe(II) oxidation and Fe (oxyhydr)oxides precipitation, subsequently reduced to iron sulfides

* Corresponding author at: Institut des Sciences de la Terre, Universite de Lausanne, Lausanne, 1015, Switzerland.
E-mail address: juliette.dupeyron@unil.ch (J. Dupeyron).

https://doi.org/10.1016/j.epsl.2023.118070
0012-821X/© 2023 The Author(s). Published by Elsevier B.V. This is an open access article under the CC BY license (http://creativecommons.org/licenses/by/4.0/).

(Rouxel et al., 2005). The evolution to positive δ^{56}Fe values during Paleoproterozoic was proposed to reflect the onset of oxidative weathering in the wake of the GOE and increased sulfate delivery to the ocean. Alternatively, the observed negative δ^{56}Fe values could reflect the onset of DIR-bacteria, which use ferric iron as an electron acceptor and release light Fe(II) to sediment porewater, from which light pyrite can precipitate (Johnson et al., 2008). Kinetic effects during pyrite precipitation from aqueous FeS precursors could also drive δ^{56}Fe variability, with Fe isotope fractionations as low as -3‰ produced during abiotic pyrite precipitation (Guilbaud et al., 2011). The expression of kinetic *versus* equilibrium effects during pyrite precipitation is controlled by the Fe/S ratio and the availability of organic material (Mansor and Fantle, 2019). The formation of pyrite follows a complex crystallization pathway with several steps and various soluble and insoluble precursors (Rickard et al., 2017) that can obscure Fe isotope composition record. Recently, Heard and Dauphas (2020) compiled bulk δ^{56}Fe values in 3.3 to 1.8 Ga-old pyrite, and highlighted a secular evolution. From Archean through the GOE, δ^{56}Fe values are mostly negative and progressively increase, before reaching positive values after the GOE. This trend, combined with the evolution of iron formation δ^{56}Fe and S isotope compositions in sedimentary sulfide from early Archean to late Paleoproterozoic, was proposed to reflect Fe and S availability control over δ^{56}Fe, and to point to a kinetically driven pyrite precipitation indirectly linked to the redox change of the ocean. Most of these previous studies have focused on millimeter-scale pyrite selected for bulk δ^{56}Fe measurement, as large grains are more easily mechanically extracted from their matrix. However, this approach may introduce a sampling bias since only large visible pyrite grains are selected for analysis. Moreover, very few data in pyrite older than 3 Ga are available from bulk measurement, leaving most of the Archean period uncovered. *In situ* analyses of pyrite at the micrometer scale allow to study a larger variability of samples, even in rocks with limited amount of pyrite grains. Microscale δ^{56}Fe values previously measured in Precambrian pyrite show a wide range, including positive values throughout the Archean (*e.g.*, Yoshiya et al., 2012; Agangi et al., 2015; Yoshiya et al., 2015b; Marin-Carbonne et al., 2014, 2020), potentially controlled by local environmental variations (*e.g.* Decraene et al., 2021b). *In situ* δ^{56}Fe database might bring new perspective on the Fe isotope variations in Archean and Paleoproterozoic pyrite. In the present contribution, we report the first compilation of *in situ* Fe isotope compositions in pyrite, throughout Archean and Paleoproterozoic. Our compilation includes data from previous studies (Table S1), as well as new data from the Francevillian Group (2.2-2.06 Ga, Gabon), Turee Creek Formation (2.43 Ga, Australia), Tumbiana Formation (2.7 Ga, Australia), Mapepe Formation (3,2 Ga) and Buck Reef Formation (3.4 Ga, South Africa) (see supplementary materials). From this dataset, we evaluate the effect of metamorphic and lithological variations and revisit the evolution of Fe isotope composition through the Precambrian.

Box 1: Iron isotope geochemistry

Iron has four stable isotopes: ^{54}Fe, ^{56}Fe, ^{57}Fe and ^{58}Fe, with the varying abundance of 5.8%, 91.7%, 2.2% and 0.3%, respectively. The isotope compositions are reported in the usual delta notation (δ) in permil (‰), relative to the international standard IRMM-014 (Institute for Reference Materials and Measurements):

$$\delta^{5x}\mathrm{Fe} = \left(\frac{^{5x}\mathrm{Fe}/^{54}\mathrm{Fe}_{sample} - ^{5x}\mathrm{Fe}/^{54}\mathrm{Fe}_{IRMM-014}}{^{5x}\mathrm{Fe}/^{54}\mathrm{Fe}_{IRMM-014}}\right) \times 1000 \quad (1)$$

where x is 6, 7 or 8. Fe isotope composition is usually only expressed as δ^{56}Fe, as most isotope variations are mass-dependent (*e.g.*, Dauphas et al., 2017). The variability of isotope compositions in natural reservoirs is inherited from isotopic exchanges during chemical and/or physical reactions. This includes various processes such as redox reactions, mineral precipitation, adsorption onto mineral or biological surfaces, organic complexation and/or biological uptake. Isotope fractionations can occur at equilibrium, in which case the reactant and product can freely exchange isotopes. This is typically the case of aqueous Fe(II)-Fe(III) exchanges, which are particularly rapid (*i.e.*, a few seconds; Welch et al., 2003). Alternately, unidirectional processes and off-equilibrium reactions are accompanied by kinetic isotope fractionation. Mineral precipitation under specific conditions can be kinetically controlled, as illustrated in the case of hematite (Skulan et al., 2022) and iron sulfide precipitation (Guilbaud et al., 2011). The largest iron isotope fractionations are observed during redox reactions, iron oxidation (Croal et al., 2004) and reduction (Crosby et al., 2005). Iron isotope fractionations of various physico-chemical processes have recently been reviewed in Dauphas et al. (2017) and Johnson et al. (2020).

Box 2: Comparison of Fe isotope analytical methods

Iron isotope analyses were first performed by thermal ionization mass spectrometry (TIMS). These early works suffered from poor thermal ionization efficiency of Fe and variable instrumental mass fractionation during measurement (Johnson et al., 2020).

Nowadays, multi-collector inductively coupled-plasma mass spectrometry (MC-ICP-MS) is widely used for iron isotope analysis. Benefits of this method include high ionization efficiency of iron by argon plasma, and stable instrumental mass fractionation which can be corrected for by sample-standard bracketing (Dauphas and Rouxel, 2006). Sample preparation for MC-ICP-MS measurement of iron isotopes involves mineral separation from the matrix, dissolution and separation of Fe by ion-exchange chromatography. Mineral separation can be performed chemically, by sequential extraction of the various iron-bearing mineral phases (Huerta-Diaz and Morse, 1990; Poulton and Canfield, 2005), or by mineral grain separation such as rock crushing and grain handpicking (Rouxel et al., 2005). With this approach, Fe isotope composition can be measured with a precision of 0.1‰/amu (Dauphas et al., 2017).

Alternatively, iron isotope analyses can be performed by *in situ* measurement on mineral grains using secondary ion mass spectrometry (SIMS) and ns- or fs-laser ablation MC-ICP-MS (LA-MC-ICP-MS). These techniques allow for sputtering of the mineral of interest at the sample surface and subsequent isotope analysis. For iron isotope analysis by SIMS, the primary ion beam is typically focused to a 15 µm-diameter spot, sputtering the sample surface over a zone of 3 to 10 µm and forming a pit from less than 1 µm to a few µm in depth (Marin-Carbonne et al., 2020; Decraene et al., 2021a). Reproducibility better than 0.2‰ (2σ, ^{56}Fe/^{54}Fe) can be achieved (Galić et al., 2017; Marin-Carbonne et al., 2020; Decraene et al., 2021a). The laser spot diameter during fs-LA analysis is similar to that of the primary ion beam, however the pit depth can be up to tens of µm, resulting in 6-fold higher sample consumption with a similar reproducibility (Zheng et al., 2018).

2. Material and methods

2.1. Data compilation

Both published and new *in situ* Fe isotope compositions of iron sulfides from Archean to Proterozoic were compiled (see the supplementary materials). The measurements were performed by secondary ion mass spectrometer (SIMS), or laser ablation multi-collector inductively coupled plasma mass spectrometer (LA-MC-ICP-MS). New data were measured on samples from two IPGP drill-cores (TCDP1 and PPDP2), from the BARB3 drillcore (ICDP, 2008) and the Francevillian Group. All samples are described in the supplementary materials. The compilation primarily includes the age, size and morphology of pyrite together with the lithology of the host rock (Table S1). The metamorphic grade and organic matter content were also compiled when available.

2.2. SIMS analyses

Iron isotope compositions were measured with a Cameca ims 1270 ion microprobe at CRPG-CNRS (Nancy, France) for TCDP samples, at UCLA (Los Angeles, USA) for BARB3 samples, and with a Cameca 1280 HR at the SwissSIMS (Lausanne, Switzerland) for the samples from the Francevillian Group, following the procedures described in Marin-Carbonne et al. (2011) and Decraene et al. (2021a). Pyrite grains were sputtered by a $^{16}O^-$ primary beam of 10 nA intensity focused to a spot of about 10 to 15 µm. $^{54}Fe^+$ and $^{56}Fe^+$ were measured in multi-collection mode with two off-axis Faraday cups, with a mass resolving power of ~7,000. The isobaric interference of ^{54}Cr on ^{54}Fe was monitored at masses 52 and 53, but chromium levels were negligible in all samples. The internal precision for $\delta^{56}Fe$ values was typically better than ± 0.1‰ (2σ), and the external reproducibility based on multiple measurements of our pyrite reference material (Balmat with $\delta^{56}Fe$ = -0.399‰) was better than ±0.2‰ (2σ).

2.3. Statistical analysis

The database presented in this study comprises isotope compositions reported in 12 scientific publications, in addition to our new data (see supplementary material). All data are considered, without being filtered, although the contributions of each publication are unequal among the studies and/or geological formations (from 16 to more than 200 reported $\delta^{56}Fe$ values). Iron isotope compositions are displayed as distributions, in the form of histogram and often probability density. The former allows to appreciate the amount of data per bin, while the latter is necessary as it reflects both measurement values and errors, which are different for SIMS and LA-MC-ICP-MS. Gaussian function was used for probability density calculation (Equation (2), where μ is the expected value and σ the standard deviation).

$$f(x) = \frac{1}{\sigma\sqrt{2\pi}} e^{-\frac{1}{2}(\frac{x-\mu}{\sigma})^2} \quad (2)$$

For histograms and probability density distributions, a small bin size was carefully chosen, so that the distributions do not vary with bin boundaries. However, the small bin size adopted here can induce minor peaks that might not be representative. Histograms and probability density distributions are shown with 0.15‰ bin size, in a range from -5.5 to +5.5‰. Finally, the nonparametric Mann Whitney U test was used to evaluate the probability of two independent non-gaussian distributions to be equal.

3. Results

About 2000 Fe isotope compositions of synsedimentary or diagenetic pyrite grains were compiled, with values between -4.87 and +5.04‰ (Fig. 1, Table 1). This wide range is roughly constant throughout the studied interval (3.8 to 1.8 Ga). The widest range is observed between 2.8 and 2.6 Ga, concomitantly with the GOE, but it can simply reflect the large number of available data (1/3 of the data were measured in 2.8 to 2.6 Ga-old pyrite). The medians show no specific time evolution (Fig. 1), strongly contrasting with those compiled for bulk $\delta^{56}Fe$ values of pyrites (Heard and Dauphas, 2020).

Information on the pyrite grain size was not available in all previous publications. Among the grains for which the size was specified, most of them are millimeter-sized (Fig. 3). These large grains have $\delta^{56}Fe$ values ranging from -4 to +4‰, with most values clustering between -2 and +2‰. $\delta^{56}Fe$ values of 0.1 to 1 mm-sized grains range from -3 to +1.5‰. Mid-size (50 to 100 µm) grains are mostly positive, with values up to +3‰, while small (<50 µm) grains span a $\delta^{56}Fe$ from -2 to +4‰.

Pyrite compiled in the present study experienced various metamorphic grades. The range of $\delta^{56}Fe$ values in amphibolite facies is slightly narrower compared to prehnite-pumpellyite and greenschist facies, but the corresponding number of data is also lower (316 *vs* > 700; Fig. 4).

Fe isotope composition of pyrite depends on host-rock lithology (Fig. 5). The distributions observed in stromatolites and cherts are bimodal and similar (Mann Whitney U =102113, p=0.86, two-sided). In contrast, carbonates and BIFs show a monomodal and more restricted range from -3.4 to +0.57‰ and from +0.25 to +2.35‰ respectively. Interestingly, carbonates display mostly negative values whereas BIFs exclusively contain positive values. It is worth noting that the number of analyses for these lithologies is the smallest (n=45 for carbonates, and n=90 for BIFs). Detrital sediments show a large multimodal range of distribution from -4.18 to +5.04‰.

The $\delta^{56}Fe$ temporal evolution is represented in Fig. 6 for various intervals including Eoarchean (>3.6 Ga), Paleoarchean (3.6-3.2 Ga), Mesoarchean and Neoarchean (3.2-2.8 and 2.8-2.5 Ga). Mesoarchean and Neoarchean intervals were merged because only 11 data were available for Mesoarchean pyrites, at 2.9 Ga. The Paleoproterozoic was subdivided as Siderian and Rhyacian (2.5-2.05 Ga), and Orosirian and Statherian (2.05-1.6 Ga). Data in the Eoarchean and Paleoproterozoic time bins only include 1 or 2 locations, while data in the Paleo-, Meso- and Neoarchean intervals comprise 8 different locations, therefore being statistically more robust. During Eoarchean, a negative and two positive modes are observed, around -1, 0.75 and 1.8‰. In the Paleoarchean, negative values are mostly comprised between 0 and -2‰, with a mode centered around -1.5‰, and one main positive mode is observed at 0.75‰. Between Mesoarchean and Neoarchean, the negative mode at -1.5‰ is preserved, while the positive one becomes larger, encompassing $\delta^{56}Fe$ values from 0 to 1‰. A 0-centered mode becomes distinct between 2.5 and 2.05 Ga, as the positive and negative modes shift to values of 2.25 and -2.5‰, respectively. In the late Paleoproterozoic, the $\delta^{56}Fe$ range turns into a monomodal distribution, with a main peak around -0.75‰. An important observation is that the positive mode is dominant in the $\delta^{56}Fe$ distributions from Paleoarchean, Mesoarchean, Neoarchean, and the first half of the Paleoproterozoic.

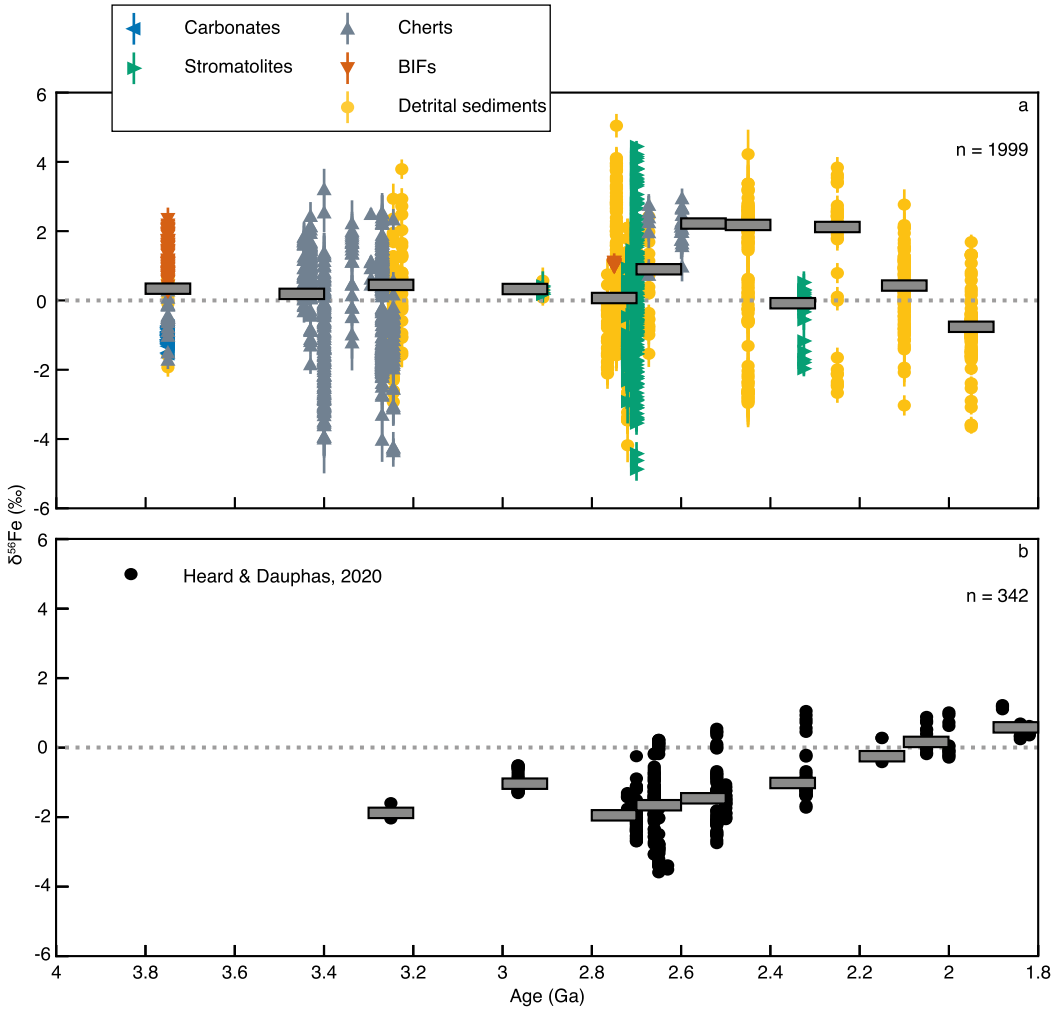

Fig. 1. Archean and Paleoproterozoic sedimentary δ^{56}Fe records. (a) δ^{56}Fe compilation of this study, classified by lithology. The δ^{56}Fe values were measured by *in situ* analytical methods. (b) Adapted from Heard and Dauphas (2020). The δ^{56}Fe values were acquired by bulk conventional techniques. The number of analyses (n) is reported for each study. Medians are plotted as time-bins of 100 Ma.

4. Discussion

4.1. Discrepancy between bulk and in situ δ^{56}Fe evolution

The large and constant range observed for the secular evolution of *in situ* pyrite δ^{56}Fe values (Fig. 1) is at odds with the shift from negative to positive values visible in the bulk δ^{56}Fe compilation from Archean to late Paleoproterozoic (Heard and Dauphas, 2020). For pyrite older than 2.96 Ga, a comparison between bulk and *in situ* δ^{56}Fe values is meaningless, due to the difference in number of data (4 *vs* 690). The distinct negative δ^{56}Fe excursion between 2.7 and 2.5 Ga determined from bulk analyses has no equivalent in *in situ* data. This discrepancy could arise from a loss of spatial δ^{56}Fe heterogeneity when preparing samples for bulk analyses (Yoshiya et al., 2015b). Alternatively, it may reflect a sampling bias. Large pyrite grains are routinely analyzed in the case of bulk measurements, as those are easily extracted from their matrix. The compilation presented by Heard and Dauphas (2020) almost exclusively includes millimeter-scale pyrite grains, largely hosted in black shales (see Rouxel et al., 2005; Archer and Vance, 2006; Hofmann et al., 2009; Busigny et al., 2017; Eickmann et al., 2018). In contrast, *in situ* techniques allow the measurement of smaller pyrite grains, at the micrometer-scale, in any type of sedimentary lithology (*e.g.,* Whitehouse and Fedo, 2007; Nishizawa et al., 2010; Yoshiya et al., 2012; Marin-Carbonne et al., 2014; Agangi et al., 2015; Virtasalo et al., 2015; Yoshiya et al., 2015a,b; Galić et al., 2017; Czaja et al., 2018; Marin-Carbonne et al., 2020; Decraene et al., 2021b).

The differences observed in the two compilations can therefore arise from sample bias. Pyrite δ^{56}Fe is tied to lithology (Fig. 5), as illustrated by the offset between δ^{56}Fe datasets measured in pyrite originating from different lithologies. An offset of 2.4‰ is observed between median δ^{56}Fe values measured by bulk and *in situ* techniques in black shales *versus* sandstone and mudstone, respectively, in Jeerinah Formation (2.7 Ga, Western Australia, Fig. 2a). Furthermore, comparing millimeter pyrite of roughly the same age (~2.7 Ga) reveals that bulk and *in situ* analyses of black shale-hosted pyrite are consistent, contrasting with δ^{56}Fe values measured in quartz pebble-hosted pyrite (Fig. 2b). Various pyrite grain size and morphology can record different formation processes within the same lithologies, with millimeter grains mostly recrystallized during diagenesis or metamorphism (Marin-Carbonne et al., 2014, 2020), while micropyrite can record sedimentary origin (Marin-Carbonne et al., 2020; Decraene et al., 2021b; Marin-Carbonne et al., 2022). Hence, grain size could be an additional cause for sample bias, although not detectable from the data compiled herein (Fig. 3). These aspects should be further explored in the future, by combining both *in situ* and bulk isotopic analyses on the same rock samples.

Table 1
List of geological locations from which pyrite grains were sampled, the corresponding number of analyses, and references in which the data were published, per time interval used in Fig. 6. References are given by location.

Time interval (Ga)	Locations	Number of analyses	References
3.8 - 3.6	Isua Greenstone Belt	178	Yoshiya et al. (2015a) Whitehouse and Fedo (2007)
3.6 - 3.2	Hooggenoeg Complex	37	Yoshiya et al. (2015b)
	Noisy Complex	94	Yoshiya et al. (2015b)
	Buck Reef	145	This study
	Kromberg Complex	23	Yoshiya et al. (2015b)
	Mendon Formation	227	Galić et al. (2017) Marin-Carbonne et al. (2020) This study
	Mapepe Formation	156	Galić et al. (2017) This study
	Fig Tree Group	5	Yoshiya et al. (2015b)
	Moodies Group	33	Yoshiya et al. (2012)
3.2 - 2.5	Nsuze Group	11	Nishizawa et al. (2010)
	Bubi Greenstone Belt	35	Marin-Carbonne et al. (2014)
	Wilgie Mia Formation	13	Czaja et al. (2018)
	Ventersdorp Contact Reef	121	Agangi et al. (2015)
	Tumbiana Formation	430	Nishizawa et al. (2010) Yoshiya et al. (2012) Decraene et al. (2021b) This study
	Maddina Formation	19	Nishizawa et al. (2010)
	Jerrinah Formation	35	Nishizawa et al. (2010) Yoshiya et al. (2012)
	Marra Mamba Formation	17	Nishizawa et al. (2010) Yoshiya et al. (2012)
2.5 - 2.05	Turee Creek Formation	181	Nishizawa et al. (2010) This study
	Francevillian Formation	101	This study
2.05 - 1.8	Talvivaara Formation	138	Virtasalo et al. (2015)

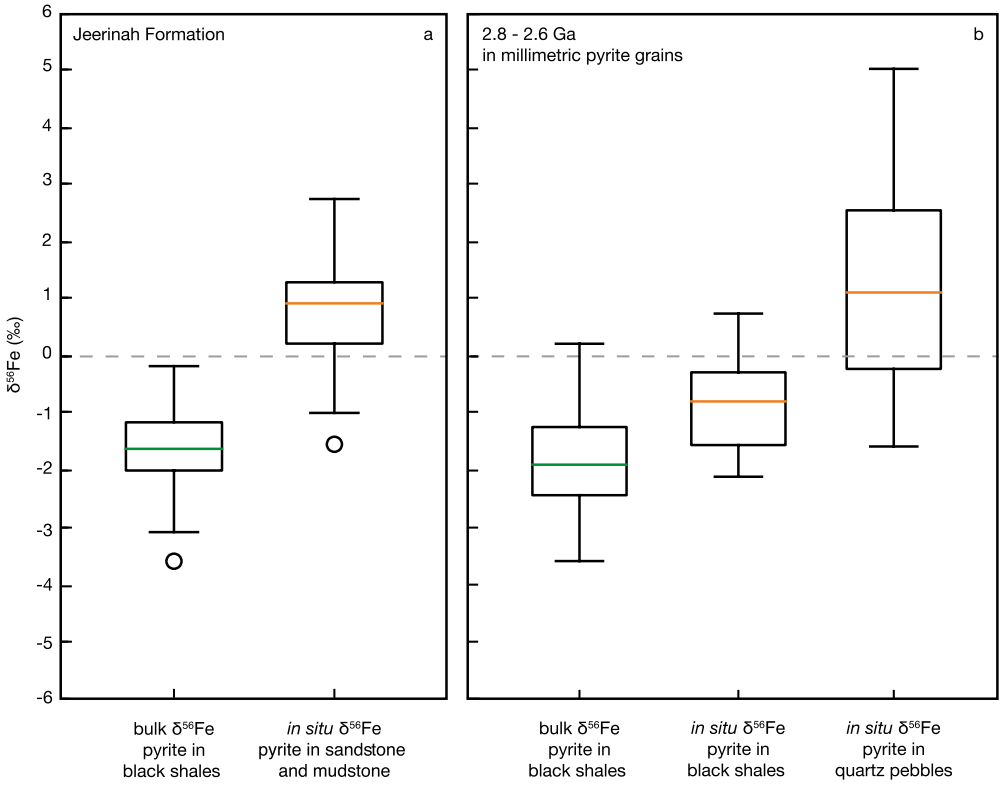

Fig. 2. Bulk and *in situ* δ^{56}Fe values measured in (a) pyrite from Jeerinah Formation (~ 2.66 Ga), and in (b) ~2.7 Ga-old millimeter pyrite hosted in black shales and quartz pebbles from several formations. In Jeerinah Formation, bulk δ^{56}Fe values (n = 70) were measured in black shale-hosted pyrite, and *in situ* δ^{56}Fe values (n = 35) in pyrite hosted in siliceous mudstone and sandstone, with little information on grain size. Millimeter pyrites around 2.7 Ga analyzed by bulk methods were hosted in black shales (n = 155, originating from 6 formations, see Heard and Dauphas (2020), while those analyzed by *in situ* techniques were hosted in both black shales (n = 35, Bubi Greenstone Belt) and quartz pebbles (n = 113, Ventersdorp Reef Contact in Kaapvaal Craton).

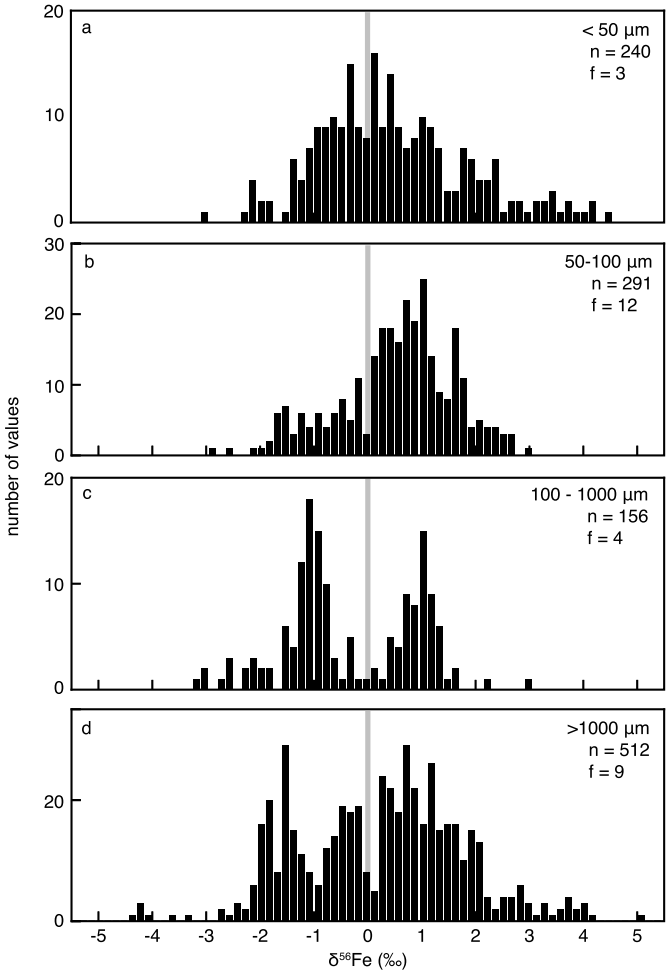

Fig. 3. Pyrite δ^{56}Fe distributions as a function of pyrite grain size. Four groups are differentiated: (a) grains with size <50 µm, (b) grains with size comprised between 50 and 100 µm, (c) grains with size of a few hundreds of microns, and (d) millimeter grains. Information on pyrite grain size was not systematically available in previous publications. Further detail on grains with size comprised between 100 and 1000 µm was not always available. The numbers of values (n) and geological formations (f) are indicated for each histogram. The vertical grey bar represents a δ^{56}Fe value of 0‰ and is drawn to facilitate comparison between plots.

4.2. Limited influence of metamorphism on pyrite iron isotope composition

Pyrite samples considered in the present compilation experienced various metamorphic grades, from prehnite-pumpellyite to amphibolite facies conditions. Hence, the effect of post-depositional metamorphism on δ^{56}Fe values must be assessed. At high temperature, isotope exchange can proceed and eventually reach equilibrium. This type of exchange homogenizes isotope ratios, leading to narrow Fe isotope distributions (Hyslop et al., 2008). The large δ^{56}Fe variability observed in pyrite from all metamorphic grades (Fig. 4) indicates that it has not been reset, as also suggested in previous SIMS studies (Whitehouse and Fedo, 2007; Galić et al., 2017; Marin-Carbonne et al., 2020). However, decreasing standard deviation with increasing metamorphic grade may reflect a slight influence of metamorphism. For the amphibolite facies, most data were obtained from a small number of samples from the Isua Greenstone Belt (3.8 Ga, Greenland) and the Talvivaara Formation (1.95 Ga, Finland), which may not be widely representative. Interestingly, both modes are present in the δ^{56}Fe distribution of pyrite from the Isua Greenstone Belt (Fig. 6a, b). This bimodality can hardly be explained by a unique process, such as metamorphism. Therefore, we conclude that primary pyrite δ^{56}Fe signatures were likely preserved in Archean and Proterozoic rocks, even in those which experienced amphibolite-facies metamorphism.

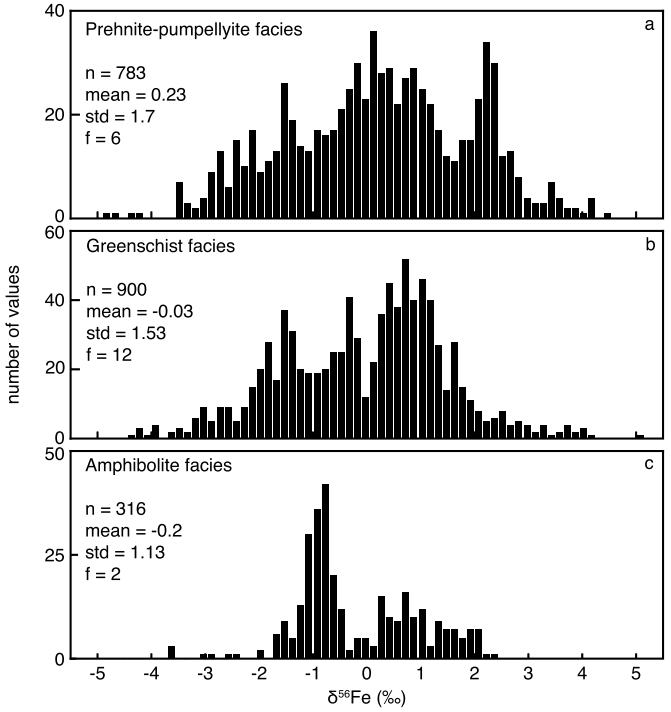

Fig. 4. Pyrite δ^{56}Fe distributions as a function of metamorphic grade. The number of values (n), mean value, standard deviation (std) and the number of geological formations (f) from which pyrite originates are indicated for each histogram.

4.3. Pyrite records partial iron oxidation

Strictly positive δ^{56}Fe values are observed in pyrite from BIFs (Fig. 5), most likely reflecting Fe-(oxyhydr)oxides reduction in the sediments and sulfidation. In detail, aqueous Fe(II) was first supplied to the ocean by hydrothermal vents with δ^{56}Fe of -0.5 to +0.1‰ (Rouxel et al., 2005), or by continental weathering (Decraene et al., 2021b). Fe(II) from the deep waters was transferred upwards by upwelling and ocean circulation, where it could be partially oxidized by photo-oxidation, by photosynthetically produced O_2, and/or by anoxygenic photosynthesis (Dauphas et al., 2004; Bekker et al., 2010; Konhauser et al., 2017). Aqueous Fe(III) readily precipitated as iron (oxyhydr)oxide, with an apparent isotope fractionation of +1 to +1.5‰ (Bullen et al., 2001; Croal et al., 2004; Nie et al., 2017), producing positive Fe isotope compositions as commonly measured in BIF Fe (oxyhydr)oxides (Planavsky et al., 2012; Dauphas et al., 2017). In this context, BIF pyrite grains could form through complete heavy Fe (oxyhydr)oxides sulfidation, thus retaining their initial positive isotope composition. Positive δ^{56}Fe modes are also present in the distributions of stromatolites and cherts, and we suggest that the corresponding pyrite particles derive from heavy Fe-(oxyhydr)oxides. In summary, positive Fe isotope compositions in BIFs, stromatolites and cherts from various geological formations point to partial aqueous Fe(II) oxidation in the Archean oceans, a phenomenon which was often suggested in the literature (*e.g.*, Ostrander et al., 2022). The compilation presented here implies that this mechanism likely existed as early as 3.8 Ga, in good agreement with bulk rock analyses of metamorphic Iron Formations from Greenland (Dauphas et al., 2004; Czaja et al., 2013).

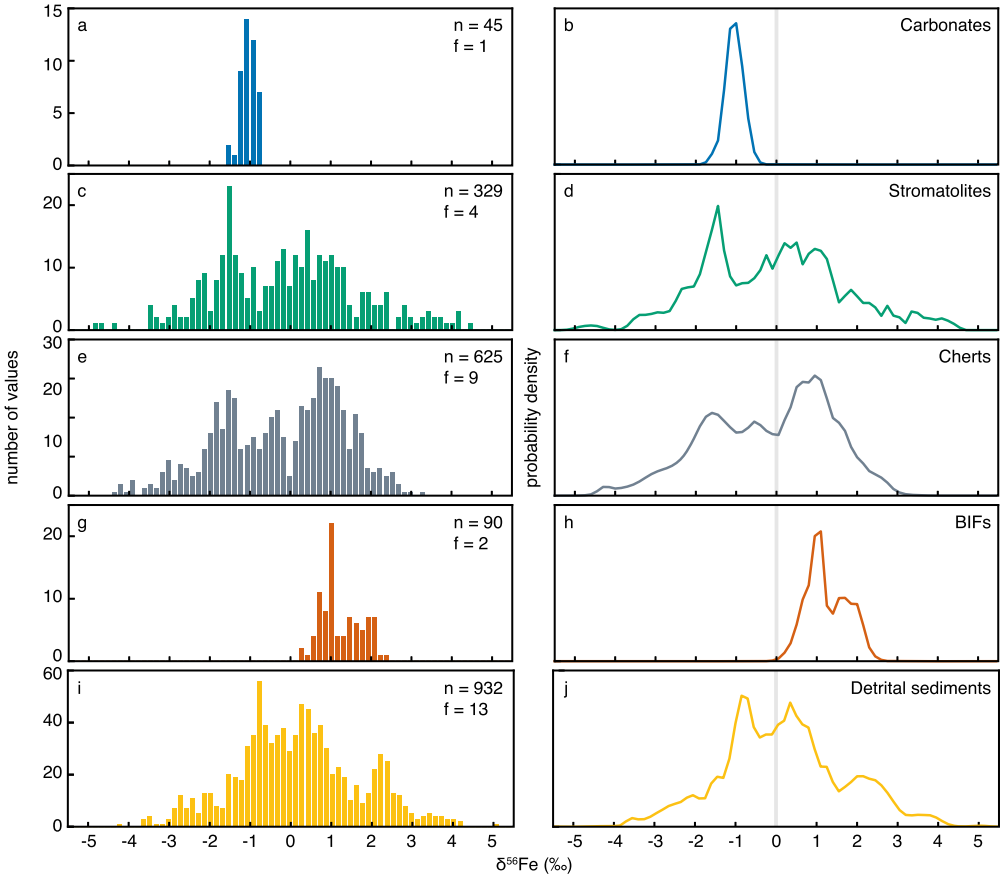

Fig. 5. Pyrite δ^{56}Fe distributions in carbonates (a, b) stromatolites (c, d), cherts (e, f), BIFs (g, h), and detrital sediments (i, j). The distributions are shown as histograms (a, c, e, g, i) and the corresponding probability density plots (b, d, f, h, j). The numbers of values (n) and geological formations (f) from which pyrite originates are indicated on the histograms. The vertical grey bar on the right panels represents a δ^{56}Fe value of 0‰ and is drawn to facilitate comparison between plots. Stromatolite distribution includes data measured in pyrite grains hosted in stromatolitic carbonate, stromatolite and stromatolitic chert (see data_compilation.xlsx in supplementary materials). Similarly, the chert distribution includes data measured in pyrite hosted in (black or white) chert, chert with barite, amphibole-rich cherts. The detrital sediment distribution includes data measured in pyrite hosted in (green, grey, black, calcareous or tuffaceous) mudstone, black shale, diamictite, (siliceous, calcareous or tuffaceous) sandstone, quartz-pyrite pebble, carbonaceous shale, carbonate laminated siltstone, quartz-rich clastic sedimentary rock and conglomerate.

4.4. Pyrite records Fe kinetic abiotic and microbial processes

Iron isotope composition in pyrite from all ages displays a negative δ^{56}Fe mode ranging from -2 to -1‰ (Fig. 6). Three main hypotheses could potentially explain such negative δ^{56}Fe values in pyrite and are discussed below.

First, Rouxel et al. (2005) proposed that partial oxidation and precipitation of large amounts of seawater Fe(II) as isotopically heavy iron (oxyhydr)oxides would leave a pool of light residual dissolved Fe(II) from which pyrite precursors could precipitate. This model implies that pyrite and iron (oxyhydr)oxide should record parallel distillation trends from heavy to light isotope compositions (Heard and Dauphas, 2020). As described in subsection 4.3, pyrite with positive δ^{56}Fe values probably retains the composition of its iron (oxyhydr)oxide precursor. Thus, the shift in opposite directions of the positive and negative δ^{56}Fe modes between the 3.2-2.5 and 2.5-2.05 Ga intervals (Fig. 6) does not support this formation mechanism. However, data from the latter interval come from only two different locations. Therefore, distillation of the seawater Fe(II) reservoir as a contributor to pyrite formation mechanism cannot completely be ruled out.

Secondly, non-redox kinetic reactions could account for a large part of the negative pyrite Fe isotope compositions (Guilbaud et al., 2011; Heard and Dauphas, 2020). Variable pyrite precipitation rate can induce large isotopic fractionation range (Guilbaud et al., 2011; Mansor and Fantle, 2019). δ^{56}Fe values as low as -3‰ are obtained when the precipitation rate is faster than the isotope exchange (Mansor and Fantle, 2019). Pyrite precipitation rate depends on Fe/S ratio, whose variation controls the kinetic *vs* equilibrium extents. In the early Archean ocean, pyrite precipitation was likely slow, due to limited sulfide availability (Mansor and Fantle, 2019). Increased sulfate delivery imparted by the GOE (Lyons et al., 2014) would have increased pyrite precipitation rate and could potentially explain the shift of the negative δ^{56}Fe mode to more negative values between 3.2 and 2.05 Ga. However, large variations of S isotope composition were reported in Archean stromatolites, pointing to local enrichments in sulfate (Bontognali et al., 2012; Marin-Carbonne et al., 2018). Following Mansor and Fantle (2019), such conditions should lead to markedly negative pyrite Fe isotope compositions in stromatolites, which are not observed (Fig. 5). For other lithologies, like cherts, carbonates and detrital sediments, the sulfate content is poorly constrained (Halevy, 2013). Therefore, a kinetic control cannot be excluded in these environments. Kinetically precipitated pyrites are expected to show a correlation between particle size and Fe isotope composition (Mansor and Fantle, 2019), which is not observed from the present compilation (Fig. 3). Similar conclusions were drawn by Decraene et al. (2021b) on micropyrite from the Tumbiana Formation. Kinetic precipitation should produce a specific isotope profile within a single pyrite grain. Precipitation rate is predicted to slow down as the reaction proceeds (Mansor and Fantle, 2019), thus δ^{56}Fe values should gradually increase from light to heavy isotope composition, from inner to outer parts of the pyrite crystal. Such Fe isotope profiles are not observed in pyrite from Mendon black

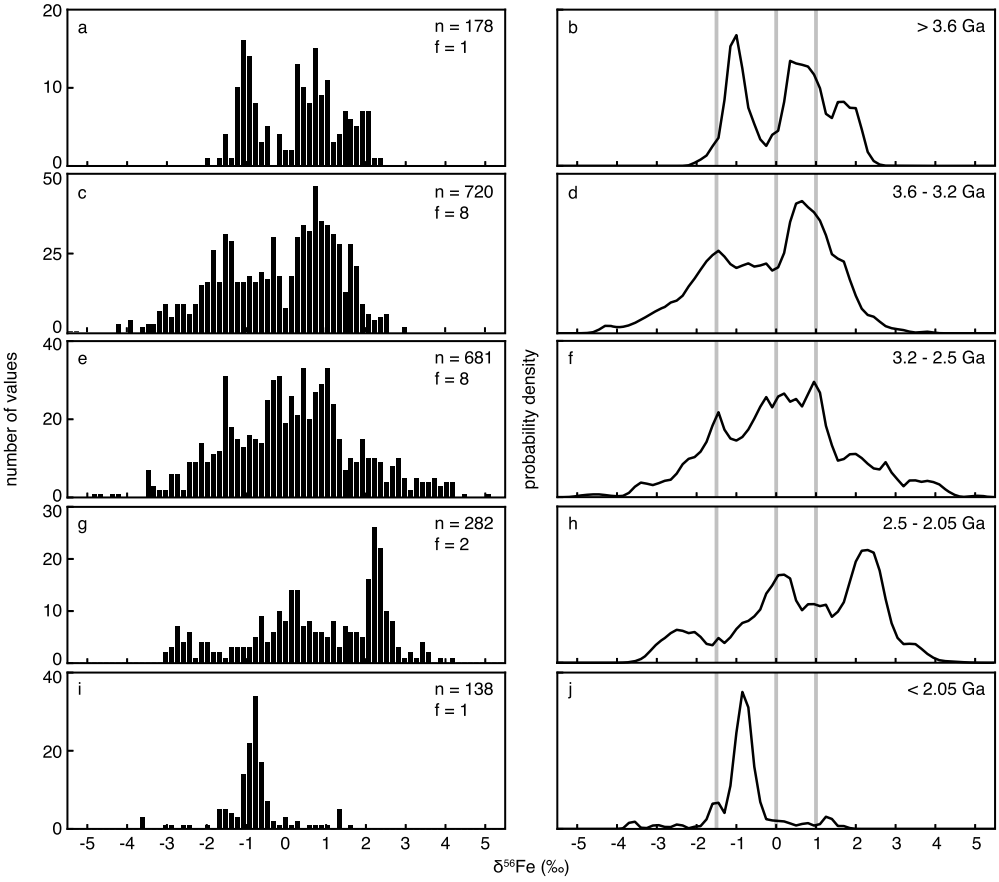

Fig. 6. Evolution of pyrite δ^{56}Fe distribution over time, shown as histograms (a, c, e, g, i) and the corresponding probability density plots (b, d, f, h, j). The numbers of values (n) and geological formations (f) from which pyrite originates are reported on the histograms. The Eoarchean and late Paleoproterozoic δ^{56}Fe distributions (a, b, and i, j) are not discussed, as they each represent only one location, Isua Greenstone Belt and Talvivaara Formation, that are both highly metamorphosed. The three vertical grey bars on the right panels represent δ^{56}Fe values of -1.5, 0 and +1‰, and are drawn to facilitate comparison between plots.

cherts (Marin-Carbonne et al., 2020). We therefore conclude that some of the pyrite grains may be produced by kinetic precipitation, but this process cannot be considered as the sole driver for pyrite formation.

Lastly, isotopically light pyrites could precipitate from partial reduction of iron (oxyhydr)oxides, either abiotically or under the influence of DIR bacteria (Crosby et al., 2007; Johnson et al., 2008; Frierdich et al., 2019). Abiotic reduction is associated with isotope fractionation between -2.6 and -3.1‰ (Wiederhold et al., 2006; Frierdich et al., 2019), not significantly different from DIR fractionation, -2.9‰ (Crosby et al., 2007). Accordingly, iron isotope fractionation alone cannot be used to assess pyrite biogenicity. Stromatolites often contain micropyrite closely associated with organic matter, likely corresponding to remains of microbial mats (Bontognali et al., 2012; Marin-Carbonne et al., 2018; Lepot et al., 2019; Decraene et al., 2021b). In our compilation, stromatolites originating from four different locations display a bimodal δ^{56}Fe distributions with a difference of -2.5‰ (Fig. 5), consistent with DIR microbial activity, of pyrite with positive δ^{56}Fe record the composition of primary Fe (oxyhydr)oxides. It may also explain the bimodal δ^{56}Fe distribution observed in cherts (Fig. 5). Specifically, organic carbon-rich cherts show mostly negative δ^{56}Fe distributions (Fig. 7). Although organic carbon in cherts is rarely measured and these results might therefore not be representative, the latter suggest that organic matter availability controls Fe reduction. Several experimental works showed that organic matter might catalyze Fe(III) reduction and pyrite formation, by providing an active surface for pyrite nucleation and therefore increasing the corresponding reaction rate (Canfield et al., 1998; Rickard et al., 2007; Rickard, 2012; Duverger et al., 2021). Consequently, organic matter availability could drive Fe isotope fractionation during pyrite precipitation. The negative Fe isotope compositions measured in carbonates could also have been produced by DIR (Fig. 5), as previously suggested by Yoshiya et al. (2012) for the Tumbiana Formation.

In summary, the negative δ^{56}Fe values cannot be explained by a single process. Partial reduction of Fe (oxyhydr)oxides followed by pyrite precipitation, alongside kinetic precipitation from dissolved Fe(II), could both have contributed to pyrite formation during the Archean and Paleoproterozoic.

4.5. Temporal evolution of micropyrite δ^{56}Fe values

The evolution of bulk δ^{56}Fe values in sedimentary pyrite through time has been proposed to reflect Fe/S ratio variations in seawater (Guilbaud et al., 2011; Mansor and Fantle, 2019; Heard and Dauphas, 2020). In particular, the shift from negative to positive δ^{56}Fe values from Archean to Paleoproterozoic could reflect an increase in sulfate delivery to seawater, imparted by continental oxidative weathering following the GOE (Canfield, 1998; Lyons et al., 2021). Positive correlation between Archean and Paleoproterozoic pyrite δ^{56}Fe and S isotope compositions of sulfide led Heard and Dauphas (2020) to suggest a primary control of the Fe/S ratio in the ocean on Fe isotope signatures in pyrite.

Our compilation of *in situ* data shows a different pattern (Fig. 1). The quasi-systematic prominence of the positive mode suggests that pyrite was mostly formed via Fe (oxyhydr)oxide reduction, starting 3.6 Ga ago. As oxidative weathering after the GOE likely

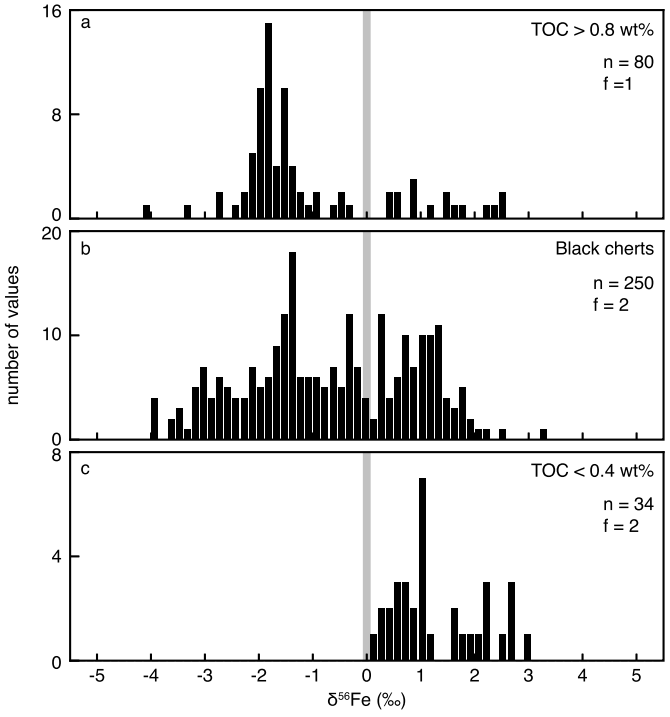

Fig. 7. Pyrite δ^{56}Fe distributions in cherts with variable total organic carbon (TOC) content. Experimental works suggested that organic matter could catalyze pyrite formation by providing active surfaces for pyrite nucleation (Rickard et al., 2007; Rickard, 2012; Duverger et al., 2021). The upper plot (a) comprises pyrite δ^{56}Fe values from cherts containing 0.82 to 1.51 wt% organic carbon. The middle plot (b) includes δ^{56}Fe values measured in black cherts for which no specific information about the organic carbon content was given. We suggest that they can reasonably be considered as organic matter-rich host rocks. In the lower plot (c), δ^{56}Fe values were measured in pyrites associated with cherts presenting TOC values from less than 0.05 to 0.38 wt%. The numbers of values (n) and geological formations (f) from which pyrite originates are indicated. Pyrite particles in organic matter-poor and organic matter-rich (TOC > 0.8 wt%) cherts have one location in common (Mendon Formation). The three other locations are distinct. The grey bar represents a δ^{56}Fe value of 0‰ and is drawn to facilitate comparison between plots.

increased the input of Fe (oxyhydr)oxide with δ^{56}Fe close to 0‰, the occurrence of 0‰ pyrite grains in stromatolites, cherts or BIFs post-dating the GOE would confirm the proposed pyrite formation mechanism from Fe (oxyhydr)oxide quantitative reduction (Section 4.3). However, only few microanalyses were carried out on such samples (only 18 analyses in 2.32 Ga old stromatolites).

Furthermore, δ^{56}Fe values close to 0‰ become more significant between 3.2 and 2.05 Ga. These values were measured in pyrite grains hosted in detrital sediments (Fig. 5), and they are similar to the crustal average δ^{56}Fe value (Beard et al., 2003). Several studies suggest that the lithosphere might have stabilized between 3.2 and 2.5 Ga, leading to the development and thickening of the continental crust (Dhuime et al., 2015; Cawood et al., 2018). This would in turn have led to the onset of continental weathering, that was evidenced in formations as old as 3.2 Ga (Hessler and Lowe, 2006). Delivery of continental Fe(II)-bearing species through rivers before the GOE (Hao et al., 2017) could have supplied the ocean detrital pyrites delivered to the ocean. Pyrite grains from various formations (3.1 to 2.6 Ga) in Zimbabwe and Kaapvaal cratons were described as detrital by Hofmann et al. (2009), based on petrographic evidence, ages greater than the depositional age, and multiple S isotope analyses. They used Fe and S isotope compositions to constrain the pyrite origin, and suggested that δ^{56}Fe values clustering around 0‰, associated with small variations in $^{34}S/^{32}S$ ratios and S mass independent fractionations close to 0‰ reflect a crustal origin. Moreover, Agangi et al. (2015) measured Fe isotope compositions in 2.7 Ga pyrite, that they interpreted to be of detrital origin. Inclusion-rich pyrites have a high δ^{56}Fe average (2.75‰), compared to concentrically laminated pyrites (0.2‰). A detrital origin of pyrite cannot be confirmed from the present compilation as only Fe isotope compositions are available and no obvious pyrite shape or size can be used as detrital indicator.

Interpretation of δ^{56}Fe distributions in the other time intervals is uncertain and not discussed herein, as the small number of pyrite localities may induce a lack of representativity.

In summary, microscale δ^{56}Fe distributions in pyrite point to Fe (oxyhydr)oxide precursor as early as 3.6 Ga ago. In addition, an influence of continental weathering might be recorded in Fe isotope signatures from 3.2 Ga. Further investigations of the δ^{56}Fe evolution through time would increase the present database and possibly strengthen the tentative conclusions drawn here.

5. Conclusions

In situ Fe isotope compositions in Archean and Paleoproterozoic pyrite show distinct trends from those obtained by conventional bulk measurements of pyrite δ^{56}Fe values. The origin of the discrepancy between *in situ* and bulk Fe isotope signatures is not clear, and should be addressed in future works, for instance by coupling *in situ* and bulk techniques on the same samples. The δ^{56}Fe distributions in various lithologies point to several pyrite formation mechanisms: total and partial Fe (oxyhydr)oxide reduction, that could be abiotic and/or potentially microbially mediated, and kinetic pyrite precipitation from dissolved Fe(II). These mechanisms might have existed since since 3.8 Ga, as suggested by the consistent evolution of the δ^{56}Fe distributions throughout early Archean to Paleoproterozoic. The high occurrence of pyrite with positive δ^{56}Fe values indicates that Fe(III) reduction was a dominant pyrite formation pathway. Importantly, this study underlines the lack of microanalyses in specific lithologies and time intervals, that hinders robust interpretation of the isotope signature records.

CRediT authorship contribution statement

JMC, VB and JD designed the study, JMC and MND conducted the SIMS analyses, JD compiled the data. All authors have contributed to the data interpretation. JD wrote the manuscript with important contributions of all co-authors.

Declaration of competing interest

The authors declare that they have no known competing financial interests or personal relationships that could have appeared to influence the work reported in this paper.

Data availability

Data are available in the Supplementary materials.

Acknowledgements

We are thankful to Pascal Phillipot, Frantz Ossa Ossa and Axel Hofmann for providing the TCDP, Gabon, and Barberton samples, respectively. V.B. thanks the Institut Universitaire de France for funding (IUF#2017-2021). This research was supported by the European Research Council (ERC) under the European Union's Horizon 2020 research and innovation program (STROMATA, grant agreement 759289). We thank Anne-Sophie Bouvier, Florent Plane and Thomas Bovay for their SIMS expertise. The SwissSIMS is hosted by the Center for Advanced Surface Analyse, CASA, a joint facility between UNIL and EPFL. Virgil Pasquier, Itay Halevy and Claire Rollion-Bard are thanked for fruitful discussions and comments on an earlier version of this manuscript. This manuscript

benefited from comments from two anonymous reviewers, as well as editorial handling by Boswell Wing.

Appendix A. Supplementary material

Supplementary material related to this article can be found online at https://doi.org/10.1016/j.epsl.2023.118070.

References

Agangi, A., Hofmann, A., Rollion-Bard, C., Marin-Carbonne, J., Cavalazzi, B., Large, R., Meffre, S., 2015. Gold accumulation in the Archaean Witwatersrand Basin, South Africa — evidence from concentrically laminated pyrite. Earth-Sci. Rev. 140, 27–53. https://doi.org/10.1016/j.earscirev.2014.10.009.

Anbar, A.D., Rouxel, O., 2007. Metal stable isotopes in paleoceanography. Annu. Rev. Earth Planet. Sci. 35, 717–746. https://doi.org/10.1146/annurev.earth.34.031405.125029.

Archer, C., Vance, D., 2006. Coupled Fe and S isotope evidence for Archean microbial Fe(III) and sulfate reduction. Geology 34, 153. https://doi.org/10.1130/G22067.1.

Balci, N., Bullen, T.D., Witte-Lien, K., Shanks, W.C., Motelica, M., Mandernack, K.W., 2006. Iron isotope fractionation during microbially stimulated Fe(II) oxidation and Fe(III) precipitation. Geochim. Cosmochim. Acta 70, 622–639. https://doi.org/10.1016/j.gca.2005.09.025.

Beard, B.L., Johnson, C.M., Skulan, J.L., Nealson, K.H., Cox, L., Sun, H., 2003. Application of Fe isotopes to tracing the geochemical and biological cycling of Fe. Chem. Geol. 195, 87–117. https://doi.org/10.1016/S0009-2541(02)00390-X.

Bekker, A., Holland, H.D., Wang, P.L., Rumble, D., Stein, H.J., Hannah, J.L., Coetzee, L.L., Beukes, N.J., 2004. Dating the rise of atmospheric oxygen. Nature 427, 117–120. https://doi.org/10.1038/nature02260.

Bekker, A., Slack, J.F., Planavsky, N., Krapez, B., Hofmann, A., Konhauser, K.O., Rouxel, O.J., 2010. Iron formation: the sedimentary product of a complex interplay among mantle, tectonic, oceanic, and biospheric processes. Econ. Geol. 105, 467–508. https://doi.org/10.2113/gsecongeo.105.3.467.

Bontognali, T.R.R., Sessions, A.L., Allwood, A.C., Fischer, W.W., Grotzinger, J.P., Summons, R.E., Eiler, J.M., 2012. Sulfur isotopes of organic matter preserved in 3.45-billion-year-old stromatolites reveal microbial metabolism. Proc. Natl. Acad. Sci. 109, 15146–15151. https://doi.org/10.1073/pnas.1207491109.

Bullen, T.D., White, A.F., Childs, C.W., Vivit, D.V., Schulz, M.S., 2001. Demonstration of significant abiotic iron isotope fractionation in nature. Geology 29, 699. https://doi.org/10.1130/0091-7613(2001)029<0699:DOSAII>2.0.CO;2.

Busigny, V., Marin-Carbonne, J., Muller, E., Cartigny, P., Rollion-Bard, C., Assayag, N., Philippot, P., 2017. Iron and sulfur isotope constraints on redox conditions associated with the 3.2 Ga barite deposits of the Mapepe Formation (Barberton Greenstone Belt, South Africa). Geochim. Cosmochim. Acta 210, 247–266. https://doi.org/10.1016/j.gca.2017.05.002.

Canfield, D.E., 1998. A new model for Proterozoic ocean chemistry. Nature 396, 450–453. https://doi.org/10.1038/24839.

Canfield, D.E., Thamdrup, B., Fleischer, S., 1998. Isotope fractionation and sulfur metabolism by pure and enrichment cultures of elemental sulfur-disproportionating bacteria. Limnol. Oceanogr. 43, 253–264. https://doi.org/10.4319/lo.1998.43.2.0253.

Cawood, P.A., Hawkesworth, C.J., Pisarevsky, S.A., Dhuime, B., Capitanio, F.A., Nebel, O., 2018. Geological archive of the onset of plate tectonics. Philos. Trans. R. Soc. A, Math. Phys. Eng. Sci. 376. https://doi.org/10.1098/rsta.2017.0405.

Craddock, P.R., Dauphas, N., 2011. Iron and carbon isotope evidence for microbial iron respiration throughout the Archean. Earth Planet. Sci. Lett. 303, 121–132. https://doi.org/10.1016/j.epsl.2010.12.045.

Croal, L.R., Johnson, C.M., Beard, B.L., Newman, D.K., 2004. Iron isotope fractionation by Fe(II)-oxidizing photoautotrophic bacteria. Geochim. Cosmochim. Acta 68, 1227–1242. https://doi.org/10.1016/j.gca.2003.09.011.

Crosby, H.A., Johnson, C.M., Roden, E.E., Beard, B.L., 2005. Coupled Fe(II)-Fe(III) electron and atom exchange as a mechanism for Fe isotope fractionation during dissimilatory iron oxide reduction. Environ. Sci. Technol. 39, 6698–6704. https://doi.org/10.1021/es0505346.

Crosby, H.A., Roden, E.E., Johnson, C.M., Beard, B.L., 2007. The mechanisms of iron isotope fractionation produced during dissimilatory Fe(III) reduction by Shewanella putrefaciens and Geobacter sulfurreducens. Geobiology 5, 169–189. https://doi.org/10.1111/j.1472-4669.2007.00103.x.

Czaja, A.D., Johnson, C.M., Beard, B.L., Roden, E.E., Li, W., Moorbath, S., 2013. Biological Fe oxidation controlled deposition of banded iron formation in the ca. 3770Ma Isua Supracrustal Belt (West Greenland). Earth Planet. Sci. Lett. 363, 192–203. https://doi.org/10.1016/j.epsl.2012.12.025.

Czaja, A.D., Van Kranendonk, M.J., Beard, B.L., Johnson, C.M., 2018. A multistage origin for Neoarchean layered hematite-magnetite iron formation from the Weld Range, Yilgarn Craton, Western Australia. Chem. Geol. 488, 125–137. https://doi.org/10.1016/j.chemgeo.2018.04.019.

Dauphas, N., John, S.G., Rouxel, O., 2017. Iron isotope systematics. Rev. Mineral. Geochem. 82, 415–510. https://doi.org/10.2138/rmg.2017.82.11.

Dauphas, N., van Zuilen, M., Wadhwa, M., Davis, A.M., Marty, B., Janney, P.E., 2004. Clues from Fe isotope variations on the origin of Early Archean BIFs from Greenland. Science 306, 2077–2080. https://doi.org/10.1126/science.1104639.

Decraene, M.N., Marin-Carbonne, J., Bouvier, A.S., Villeneuve, J., Bouden, N., Luais, B., Deloule, E., 2021a. High-spatial-resolution measurements of iron isotopes in pyrites by secondary ion mass spectrometry using the new Hyperion-II radio-frequency plasma source. Rapid Commun. Mass Spectrom. 35, e8986. https://doi.org/10.1002/rcm.8986.

Decraene, M.N., Marin-Carbonne, J., Thomazo, C., Olivier, N., Philippot, P., Strauss, H., Deloule, E., 2021b. Intense biogeochemical iron cycling revealed in Neoarchean micropyrites from stromatolites. Geochim. Cosmochim. Acta 312, 299–320. https://doi.org/10.1016/j.gca.2021.07.020.

Dhuime, B., Wuestefeld, A., Hawkesworth, C.J., 2015. Emergence of modern continental crust about 3 billion years ago. Nat. Geosci. 8, 552–555. https://doi.org/10.1038/ngeo2466.

Duverger, A., Bernard, S., Viennet, J.C., Miot, J., Busigny, V., 2021. Formation of pyrite spherules from mixtures of biogenic FeS and organic compounds during experimental diagenesis. Geochem. Geophys. Geosyst. 22. https://doi.org/10.1029/2021GC010056.

Eickmann, B., Hofmann, A., Wille, M., Bui, T.H., Wing, B.A., Schoenberg, R., 2018. Isotopic evidence for oxygenated Mesoarchaean shallow oceans. Nat. Geosci. 11, 133–138. https://doi.org/10.1038/s41561-017-0036-x.

Frierdich, A.J., Nebel, O., Beard, B.L., Johnson, C.M., 2019. Iron isotope exchange and fractionation between hematite (α-Fe2O3) and aqueous Fe(II): a combined three-isotope and reversal-approach to equilibrium study. Geochim. Cosmochim. Acta 245, 207–221. https://doi.org/10.1016/j.gca.2018.10.033.

Galić, A., Mason, P.R., Mogollón, J.M., Wolthers, M., Vroon, P.Z., Whitehouse, M.J., 2017. Pyrite in a sulfate-poor Paleoarchean basin was derived predominantly from elemental sulfur: evidence from 3.2 Ga sediments in the Barberton Greenstone Belt, Kaapvaal Craton. Chem. Geol. 449, 135–146. https://doi.org/10.1016/j.chemgeo.2016.12.006.

Guilbaud, R., Butler, I.B., Ellam, R.M., 2011. Abiotic pyrite formation produces a large Fe isotope fractionation. Science 332, 1548–1551. https://doi.org/10.1126/science.1202924.

Halevy, I., 2013. Production, preservation, and biological processing of mass-independent sulfur isotope fractionation in the Archean surface environment. Proc. Natl. Acad. Sci. 110, 17644–17649. https://doi.org/10.1073/pnas.1213148110.

Hao, J., Sverjensky, D.A., Hazen, R.M., 2017. A model for late Archean chemical weathering and world average river water. Earth Planet. Sci. Lett. 457, 191–203. https://doi.org/10.1016/j.epsl.2016.10.021.

Heard, A.W., Dauphas, N., 2020. Constraints on the coevolution of oxic and sulfidic ocean iron sinks from Archean–Paleoproterozoic iron isotope records. Geology 48, 358–362. https://doi.org/10.1130/G46951.1.

Hessler, A.M., Lowe, D.R., 2006. Weathering and sediment generation in the Archean: An integrated study of the evolution of siliciclastic sedimentary rocks of the 3.2 Ga Moodies Group, Barberton Greenstone Belt, South Africa. Precambrian Res. 151, 185–210. https://doi.org/10.1016/j.precamres.2006.08.008.

Hofmann, A., Bekker, A., Rouxel, O., Rumble, D., Master, S., 2009. Multiple sulphur and iron isotope composition of detrital pyrite in Archaean sedimentary rocks: a new tool for provenance analysis. Earth Planet. Sci. Lett. 286, 436–445. https://doi.org/10.1016/j.epsl.2009.07.008.

Hyslop, E.V., Valley, J.W., Johnson, C.M., Beard, B.L., 2008. The effects of metamorphism on O and Fe isotope compositions in the Biwabik Iron Formation, northern Minnesota. Contrib. Mineral. Petrol. 155, 313–328. https://doi.org/10.1007/s00410-007-0244-2.

Johnson, C.M., Beard, B.L., 2006. Fe isotopes: an emerging technique for understanding modern and ancient biogeochemical cycles. GSA Today 16, 4. https://doi.org/10.1130/GSAT01611A.1.

Johnson, C.M., Beard, B.L., Roden, E.E., 2008. The iron isotope fingerprints of redox and biogeochemical cycling in modern and ancient Earth. Annu. Rev. Earth Planet. Sci. 36, 457–493. https://doi.org/10.1146/annurev.earth.36.031207.124139.

Klein, C., 2005. Some Precambrian banded iron-formations (BIFs) from around the world: their age, geologic setting, mineralogy, metamorphism, geochemistry, and origins. Am. Mineral. 90, 1473–1499. https://doi.org/10.2138/am.2005.1871.

Konhauser, K., Planavsky, N., Hardisty, D., Robbins, L., Warchola, T., Haugaard, R., Lalonde, S., Partin, C., Oonk, P., Tsikos, H., Lyons, T., Bekker, A., Johnson, C., 2017. Iron formations: a global record of Neoarchaean to Palaeoproterozoic environmental history. Earth-Sci. Rev. 172, 140–177. https://doi.org/10.1016/j.earscirev.2017.06.012.

Lepot, K., Williford, K.H., Philippot, P., Thomazo, C., Ushikubo, T., Kitajima, K., Mostefaoui, S., Valley, J.W., 2019. Extreme 13C-depletions and organic sulfur content argue for S-fueled anaerobic methane oxidation in 2.72 Ga old stromatolites. Geochim. Cosmochim. Acta 244, 522–547. https://doi.org/10.1016/j.gca.2018.10.014.

Lonergan, D.J., Jenter, H.L., Coates, J.D., Phillips, E.J., Schmidt, T.M., Lovley, D.R., 1996. Phylogenetic analysis of dissimilatory Fe(III)-reducing bacteria. J. Bacteriol. 178, 2402–2408. https://doi.org/10.1128/jb.178.8.2402-2408.1996.

Lyons, T.W., Diamond, C.W., Planavsky, N.J., Reinhard, C.T., Li, C., 2021. Oxygenation, life, and the planetary system during Earth's middle history: an overview. Astrobiology 21, 906–923. https://doi.org/10.1089/ast.2020.2418.

Lyons, T.W., Fike, D.A., Zerkle, A., 2015. Emerging biogeochemical views of Earth's ancient microbial worlds. Elements 11, 415–421. https://doi.org/10.2113/gselements.11.6.415.

Lyons, T.W., Reinhard, C.T., Planavsky, N.J., 2014. The rise of oxygen in Earth's early ocean and atmosphere. Nature 506, 307–315. https://doi.org/10.1038/nature13068.

Mansor, M., Fantle, M.S., 2019. A novel framework for interpreting pyrite-based Fe isotope records of the past. Geochim. Cosmochim. Acta 253, 39–62. https://doi.org/10.1016/j.gca.2019.03.017.

Marin-Carbonne, J., Decraene, M.N., Havas, R., Remusat, L., Pasquier, V., Alléon, J., Zeyen, N., Bouton, A., Bernard, S., Escrig, S., Olivier, N., Vennin, E., Meibom, A., Benzerara, K., Thomazo, C., 2022. Early precipitated micropyrite in microbialites: a time capsule of microbial sulfur cycling. Geochem. Perspect. Lett. 21, 7–12. https://doi.org/10.7185/geochemlet.2209.

Marin-Carbonne, J., Remusat, L., Sforna, M.C., Thomazo, C., Cartigny, P., Philippot, P., 2018. Sulfur isotope's signal of nanopyrites enclosed in 2.7 Ga stromatolitic organic remains reveal microbial sulfate reduction. Geobiology 16, 121–138. https://doi.org/10.1111/gbi.12275.

Marin-Carbonne, J., Rollion-Bard, C., Bekker, A., Rouxel, O., Agangi, A., Cavalazzi, B., Wohlgemuth-Ueberwasser, C.C., Hofmann, A., McKeegan, K.D., 2014. Coupled Fe and S isotope variations in pyrite nodules from Archean shale. Earth Planet. Sci. Lett. 392, 67–79. https://doi.org/10.1016/j.epsl.2014.02.009.

Marin-Carbonne, J., Rollion-Bard, C., Luais, B., 2011. In-situ measurements of iron isotopes by SIMS: MC-ICP-MS intercalibration and application to a magnetite crystal from the Gunflint chert. Chem. Geol. 285, 50–61. https://doi.org/10.1016/j.chemgeo.2011.02.019.

Marin-Carbonne, J., Busigny, V., Miot, J., Rollion-Bard, C., Muller, E., Drabon, N., Jacob, D., Pont, S., Robyr, M., Bontognali, T.R.R., François, C., Reynaud, S., Van Zuilen, M., Philippot, P., 2020. In situ Fe and S isotope analyses in pyrite from the 3.2 Ga Mendon Formation (Barberton Greenstone Belt, South Africa): evidence for early microbial iron reduction. Geobiology 18, 306–325. https://doi.org/10.1111/gbi.12385.

Nie, N., Dauphas, N., Greenwood, R.C., 2017. Iron and oxygen isotope fractionation during iron UV photo-oxidation: implications for early Earth and Mars. Earth Planet. Sci. Lett. 458, 179–191. https://doi.org/10.1016/j.epsl.2016.10.035.

Nishizawa, M., Yamamoto, H., Ueno, Y., Tsuruoka, S., Shibuya, T., Sawaki, Y., Yamamoto, S., Kon, Y., Kitajima, K., Komiya, T., Maruyama, S., Hirata, T., 2010. Grain-scale iron isotopic distribution of pyrite from Precambrian shallow marine carbonate revealed by a femtosecond laser ablation multicollector ICP-MS technique: possible proxy for the redox state of ancient seawater. Geochim. Cosmochim. Acta 74, 2760–2778. https://doi.org/10.1016/j.gca.2010.02.014.

Ostrander, C.M., Severmann, S., Gordon, G.W., Kendall, B., Lyons, T.W., Zheng, W., Roy, M., Anbar, A.D., 2022. Significance of 56Fe depletions in late-Archean shales and pyrite. Geochim. Cosmochim. Acta, 87–104. https://doi.org/10.1016/j.gca.2021.10.013.

Planavsky, N., Rouxel, O.J., Bekker, A., Hofmann, A., Little, C.T., Lyons, T.W., 2012. Iron isotope composition of some Archean and Proterozoic iron formations. Geochim. Cosmochim. Acta 80, 158–169. https://doi.org/10.1016/j.gca.2011.12.001.

Rego, E.S., Busigny, V., Lalonde, S.V., Philippot, P., Bouyon, A., Rossignol, C., Babinski, M., de Cássia Zapparoli, A., 2021. Anoxygenic photosynthesis linked to Neoarchean iron formations in Carajás (Brazil). Geobiology 19, 326–341. https://doi.org/10.1111/gbi.12438.

Rickard, D., 2012. Sedimentary pyrite. In: Developments in Sedimentology, vol. 65. Elsevier, pp. 233–285. https://linkinghub.elsevier.com/retrieve/pii/B9780444529893000064.

Rickard, D., Grimes, S., Butler, I., Oldroyd, A., Davies, K.L., 2007. Botanical constraints on pyrite formation. Chem. Geol. 236, 228–246. https://doi.org/10.1016/j.chemgeo.2006.09.011.

Rickard, D., Mussmann, M., Steadman, J.A., 2017. Sedimentary sulfides. Elements 13, 117–122. https://doi.org/10.2113/gselements.13.2.117.

Rouxel, O.J., Bekker, A., Edwards, K.J., 2005. Iron isotope constraints on the Archean and Paleoproterozoic ocean redox state. Science 307, 1088–1091. https://doi.org/10.1126/science.1105692.

Virtasalo, J.J., Laitala, J.J., Lahtinen, R., Whitehouse, M.J., 2015. Pyritic event beds and sulfidized Fe (oxyhydr)oxide aggregates in metalliferous black mudstones of the Paleoproterozoic Talvivaara formation, Finland. Earth Planet. Sci. Lett. 432, 449–460. https://doi.org/10.1016/j.epsl.2015.09.010.

Welch, S., Beard, B., Johnson, C., Braterman, P., 2003. Kinetic and equilibrium Fe isotope fractionation between aqueous Fe(II) and Fe(III). Geochim. Cosmochim. Acta 67, 4231–4250. https://doi.org/10.1016/S0016-7037(03)00266-7.

Whitehouse, M.J., Fedo, C.M., 2007. Microscale heterogeneity of Fe isotopes in >3.71 Ga banded iron formation from the Isua Greenstone Belt, southwest Greenland. Geology 35, 719. https://doi.org/10.1130/G23582A.1.

Wiederhold, J.G., Kraemer, S.M., Teutsch, N., Borer, P.M., Halliday, A.N., Kretzschmar, R., 2006. Iron isotope fractionation during proton-promoted, ligand-controlled, and reductive dissolution of goethite. Environ. Sci. Technol. 40, 3787–3793. https://doi.org/10.1021/es052228y.

Yoshiya, K., Nishizawa, M., Sawaki, Y., Ueno, Y., Komiya, T., Yamada, K., Yoshida, N., Hirata, T., Wada, H., Maruyama, S., 2012. In situ iron isotope analyses of pyrite and organic carbon isotope ratios in the fortescue group: metabolic variations of a Late Archean ecosystem. Precambrian Res. 212–213, 169–193. https://doi.org/10.1016/j.precamres.2012.05.003.

Yoshiya, K., Sawaki, Y., Hirata, T., Maruyama, S., Komiya, T., 2015a. In-situ iron isotope analysis of pyrites in ~3.7 Ga sedimentary protoliths from the Isua supracrustal belt, southern West Greenland. Chem. Geol. 401, 126–139. https://doi.org/10.1016/j.chemgeo.2015.02.022.

Yoshiya, K., Sawaki, Y., Shibuya, T., Yamamoto, S., Komiya, T., Hirata, T., Maruyama, S., 2015b. In situ iron isotope analyses of pyrites from 3.5 to 3.2 Ga sedimentary rocks of the Barberton Greenstone Belt, Kaapvaal Craton. Chem. Geol. 403, 58–73. https://doi.org/10.1016/j.chemgeo.2015.03.007.

Further reading

Dauphas, N., Rouxel, O., 2006. Mass spectrometry and natural variations of iron isotopes. Mass Spectrom. Rev. 25, 515–550. https://doi.org/10.1002/mas.20078.

Huerta-Diaz, M.A., Morse, J.W., 1990. A quantitative method for determination of trace metal concentrations in sedimentary pyrite. Mar. Chem. 29, 119–144. https://doi.org/10.1016/0304-4203(90)90009-2.

Johnson, C., Beard, B., Weyer, S., 2020. Iron Geochemistry: An Isotopic Perspective. Advances in Isotope Geochemistry. Springer International Publishing, Cham. http://link.springer.com/10.1007/978-3-030-33828-2.

Poulton, S.W., Canfield, D.E., 2005. Development of a sequential extraction procedure for iron: implications for iron partitioning in continentally derived particulates. Chem. Geol. 214, 209–221. https://doi.org/10.1016/j.chemgeo.2004.09.003.

Skulan, J.L., Beard, B.L., Johnson, C.M., 2022. Kinetic and equilibrium Fe isotope fractionation between aqueous Fe(III) and hematite. Geochim. Cosmochim. Acta 66, 2995–3015. https://doi.org/10.1016/S0016-7037(02)00902-X.

Zheng, X.Y., Beard, B.L., Johnson, C.M., 2018. Assessment of matrix effects associated with Fe isotope analysis using 266 nm femtosecond and 193 nm nanosecond laser ablation multi-collector inductively coupled plasma mass spectrometry. J. Anal. At. Spectrom. 33, 68–83. https://doi.org/10.1039/C7JA00272F.

Juliette Dupeyron obtained her MSc at the Institut de Physique du Globe de Paris (IPGP, France) in 2021. She is currently a PhD candidate at the University of Lausanne (UNIL, Switzerland) and IPGP, where she studies pyrite formation in modern anoxic environments. She is supervised by Johanna Marin Carbonne (UNIL), Jasmine Berg (UNIL), and Vincent Busigny (IPGP).

Marie-Noëlle Decraene graduated from the University of Lorraine (France) in 2018 and recently obtained her PhD in Earth sciences at the University of Lausanne (Switzerland). Her research focuses on the origin of pyrite in ancient microbialites. She is interested in the ability of micrometric pyrite to record and preserve microbial processes, by measuring spatially resolved Fe isotopes in Archean and Phanerozoic sedimentary rocks.

Johanna Marin Carbonne completed her PhD in geosciences at the CRPG-CNRS (University of Lorraine, France) in 2009. She was first a researcher at UCLA (USA, 2010-2012), then at the Institut de Physique du Globe de Paris (France, 2012-2014). She joined the faculty of the University Jean Monnet (Saint-Etienne, France) and the laboratory Magma and Volcanoes (Clermont Ferrand, France), and moved to the University of Lausanne (UNIL) in 2018. She is currently associate professor in stable isotope geochemistry at UNIL and the director of the SwissSIMS, an ion probe national facility owned by the University of Lausanne, University of Bern, University of Geneva and ETHZ. Her research interests include Early Earth surface condition reconstructions, redox biogeochemical cycles through time, microbialite and stromatolite formation and microbe mineral interactions.

Vincent Busigny is a Professor of Geochemistry at the University Paris Cité and the Institut de Physique du Globe de Paris. After completing his PhD in 2004 in Paris under the supervision of Marc Javoy, Pascal Philippot and Pierre Cartigny, he worked with Nicolas Dauphas at the University of Chicago before returning to France. His research emphasizes the use of stable isotopes (Fe, N, C, H, O, S) as tracers of mineral-fluid-life interactions. He currently focuses on the reconstruction of Precambrian environments and ecosystems based on three different approaches: study of ancient sedimentary rocks, laboratory experiments, and modern analogues of ancient environments. Other applications include the behavior of fluid-mobile elements during alteration and subduction of oceanic lithosphere to determine chemical evolution of terrestrial surface and mantle reservoirs.